

Three-Dimensional High-Density Hierarchical Nanowire Architecture for High-Performance Photoelectrochemical Electrodes

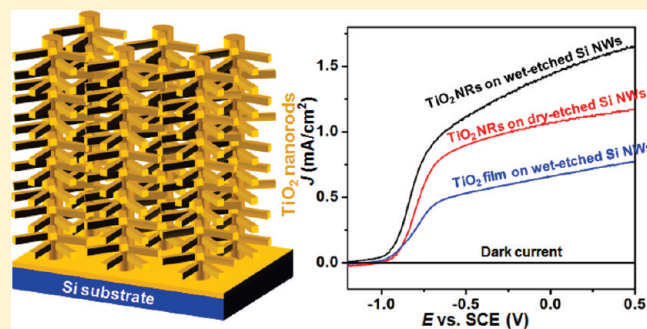
Jian Shi,[†] Yukihiro Hara,[‡] Chengliang Sun,[†] Marc A. Anderson,[‡] and Xudong Wang^{*,†}

[†]Department of Materials Science and Engineering and [‡]Civil and Environmental Engineering, University of Wisconsin-Madison, Madison, Wisconsin, United States

S Supporting Information

ABSTRACT: Three-dimensional (3D) nanowire (NW) networks are promising for designing high-performance photoelectrochemical (PEC) electrodes owing to their long optical path for efficient light absorption, high-quality one-dimensional conducting channels for rapid electron–hole separation and charge transportation, as well as high surface areas for fast interfacial charge transfer and electrochemical reactions. By growing titanium dioxide (TiO₂) nanorods (NRs) uniformly on dense Si NW array backbones, we demonstrated a novel three-dimensional high-density heterogeneous NW architecture that could enhance photoelectrochemical efficiency. A 3D NW architecture consisting of 20 μm long wet-etched Si NWs and dense TiO₂ NRs yielded a photoelectrochemical efficiency of 2.1%, which is three times higher than that of TiO₂ film–Si NWs having a core–shell structure. This result suggests that the 3D NW architecture is superior to straight NW arrays for PEC electrode design. The efficiency could be further improved by optimizing the number of overcoating cycles and the length/density of NW backbones. By implementing these 3D NW networks into electrode design, one may be able to advantageously impact PEC and photovoltaic device performance.

KEYWORDS: Titanium dioxide, nanorods, 3D nanowire network, photoelectrochemistry, water splitting



Photocatalyzed water splitting has received considerable attention as a clean, abundant and renewable strategy in which to address both the energy crisis and environmental concerns over the use of fossil fuels.^{1–8} Efficient, stable, chemically inert, low-cost, and nontoxic photoelectrochemical (PEC) electrodes are essential to the success of water splitting.^{9–16} Light absorption, charge generation and separation, and the matching of interfacial redox reactions represent the three most fundamental aspects of problems we face in this arena.^{17–24} A fast interfacial charge transfer rate and suppressed electron–hole recombination are greatly desired.^{25–27} Promising solutions for efficient solar-to-chemical energy conversion include avoiding charge trapping on semiconductor surfaces, increasing semiconductor-electrolyte interfacial area, and enhancing the capability for instantaneous charge collection, separation, and transport.^{9,12,17,20,28,29} Therefore, three-dimensional (3D) nanowire (NW) networks may represent ideal architectures for high-performance PEC electrodes. High-density treelike branched NW arrays provide a type of architecture that could offer long optical paths for efficient light absorption, high-quality one-dimensional (1D) conducting channels for rapid electron–hole separation and charge transport, as well as high surface areas for fast interfacial charge transfer and electrochemical reactions.^{4,17} In this paper, we report on the development of a 3D high-density heterogeneous NW architecture by growing titanium dioxide (TiO₂) nanorods

(NRs) uniformly on dense Si NW array backbones using our surface-reaction-limited pulsed chemical vapor deposition (SPCVD) technique.^{30,31} Dramatic increases of photocurrent and photoelectrochemical efficiency were obtained when the 3D NW architectures were applied as PEC anodes.

Fabrication of 3D TiO₂ NR-Si NW architecture is schematically illustrated in Figure 1a. First, vertical Si NW arrays were prepared by selectively etching a heavily doped n-type Si substrate. Second, high density TiO₂ NRs were uniformly grown around the Si NWs via the SPCVD process. Lastly, an additional thin film of anatase TiO₂ was coated on the NR-NW heterostructure by atomic layer deposition (ALD) to completely cover Si NW surfaces. As schematically shown in Figure 1b, when this heterogeneous structure is used as a PEC anode for water splitting, photocatalyzed H₂O oxidation reactions would only occur on the TiO₂ surfaces. In principle, the photogenerated electrons should quickly be transported through the Si NW backbone and reach the counter electrode with minimal losses owing to the high conductivity of Si NWs and isolation from electrolyte.^{20,28} The very large surface area provided by the TiO₂ NR arrays together with the high-speed electron transport channels provided by the

Received: May 29, 2011

Revised: July 10, 2011

Published: July 19, 2011

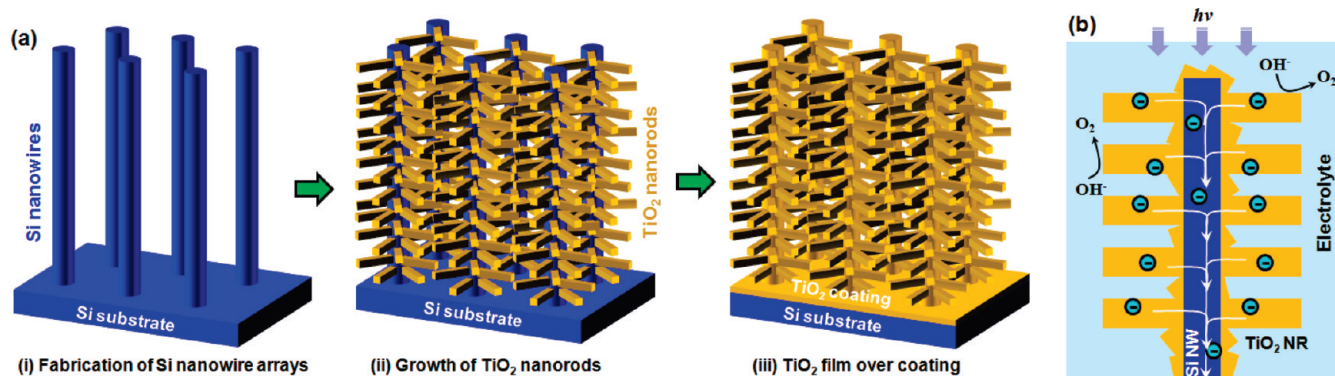


Figure 1. (a) Schematic procedures for making treelike TiO₂ NR-Si NW 3D architectures. (b) Schematic illustration of using TiO₂ NR-Si NW heterostructure as PEC anode for water splitting reactions.

Si NWs are promising features that could lead to a significant improvement of photoelectrochemical efficiency.

Driven by this rationale, Si NW backbones were first fabricated by deep reactive ion etching (RIE) technique using a self-assembled nanosphere monolayer as mask (the fabrication details are included in Supporting Information).^{32,33} N-type Si wafer (0.001–0.005 Ωcm) was used to fabricate NWs to ensure good electrical conductivity. The typical size of as-fabricated Si NWs were ~300 nm in diameter, ~15 μm long, and ~200 nm apart from each other (inset of Figure 1a). After 600 cycles of SPCVD growth (see Supporting Information for experimental details), uniform TiO₂ NRs were deposited on the entire Si NW surface. Figure 2a shows a top-view scanning electron microscopy (SEM) image of as-grown TiO₂ NRs that illustrate this feature. The NRs exhibited uniform dimensions that are 35 ± 5 nm in diameter and 252 ± 37 nm in length. All the Si NWs remained straight and no agglomeration was observed after TiO₂ NR growth (Figure 2b). Figure 2c,d shows SEM images taken at the middle and bottom regions of the cross-section, respectively, showing a uniform and dense coverage of TiO₂ NRs. This is a typical growth result across the entire sample and it provides evidence that a very large quantity of uniform-sized TiO₂ NRs can be grown on all possible surfaces despite the extremely narrow and deep spaces left in between Si NWs.

Consistent with our previous research, the as-deposited TiO₂ NRs exhibited pure anatase phase character as identified by X-ray diffraction (XRD) (Supporting Information Figure S1). All the NRs were single crystals rooted on the surface of Si NWs (Supporting Information Figure S2a). Selective area electron diffraction (SAED) (Supporting Information Figure S2b) further confirmed that the single-crystalline anatase structure and growth/surface arrangements were identical to the TiO₂ NRs grown in anodic aluminum oxide (AAO) templates.³⁰ This observation suggests that the supporting surfaces/substrates have negligible influence on the crystal structure and orientations of TiO₂ NRs.

As we reported previously, the growth of TiO₂ NRs was dictated by surface adsorption and reactions in which the partial pressure of TiCl₄ precursor played an important role. Specifically, when the partial pressure of TiCl₄ was too high, surplus supply of precursor diminishes the difference of adsorption and surface chemical reaction rates on different crystal facets of TiO₂, thereby rendering an isotropic nanoparticle growth. When the precursor supply was reduced to an appropriate level, the growth rate of the TiO₂ (001) plane became distinctly faster and thus the

crystal growth transformed to an anisotropic mode and NR morphology was received. This growth behavior observed in AAO channels also applies to the Si NW matrix. To better generalize these growth patterns, here we use pressure change (ΔP) upon 500 ms precursor pulsing (500 ms is the fixed pulsing time and ΔP is the pressure difference of chamber before and after ALD valve is on) to describe the morphology-precursor supply relationship. Nine different ΔP of TiCl₄ precursor were examined ranging from 20 to 1000 millitorr, while all the other growth parameters remained constant (500 ms pulsing time, 600 SPCVD cycles, and 600 °C). Here, ΔP was adjusted by regulating the temperature of TiCl₄ precursor. Figure 3 illustrates the change of morphology in TiO₂ NRs as a function of TiCl₄. When the ΔP was as low as 20 millitorr, TiO₂ NRs could not fully evolve and both the diameter and aspect ratio of the NRs were small (left inset of Figure 3). When ΔP was above ~160 millitorr, large crystallites were obtained indicating a superfluous supply of precursors (right inset of Figure 3). The appropriate ΔP was found between 60 to 140 millitorr as indicated by the light green zone in Figure 3. In this region, aspect ratio as high as 9 was achieved when the ΔP was 120 millitorr (central inset of Figure 3), demonstrating the ideal conditions for TiO₂ NRs growing in a high-density Si NW forest.

Dry-etched Si NWs offered a good template in which to study the growth behavior of TiO₂ NRs on Si surfaces. However, their fabrication procedures are relatively complicated and costly. In order to further apply this technique to applicable PEC electrode design on a large scale, wet-etched Si NW arrays were used for growing these NRs. In this case, Si NWs were fabricated using the same heavily doped Si wafer by the metal-assisted wet-etching technique (see Supporting Information for experimental details).²⁰ This technique can produce vertical Si NW arrays with higher density, smaller size, and a larger aspect ratio compared to the dry-etching technique (Supporting Information Figure S3). However, one should caution that assemblages or bundles of NW tips always exist due to the capillary force from etchant solution.

Under the optimized SPCVD condition (ΔP was 120 millitorr with 500 ms pulsing time), high-density TiO₂ NRs having uniform dimensions were successfully deposited on the wet-etched Si NWs. Figure 4a is a planar view of a wet-etched Si NW forest after the growth of these NRs. Tip bundling can be clearly observed. Closer examination showed that the Si NWs were very thin and exhibited irregular cross sections as highlighted by yellow dashed circles in the inset of Figure 4a. While the open spaces left within the bundling area were very small, the TiO₂

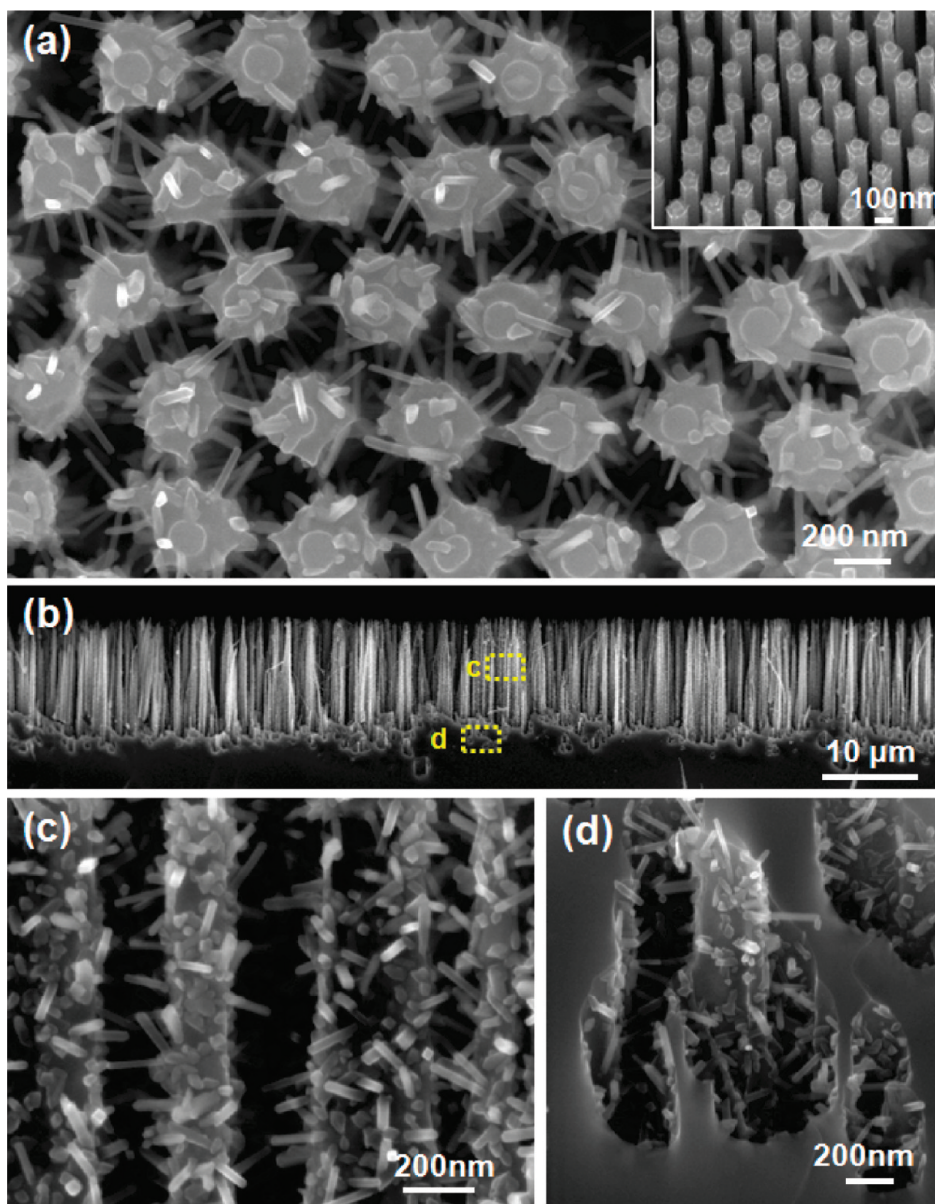


Figure 2. TiO₂ NRs grown on vertical Si NW arrays fabricated by dry etching. (a) Top view of Si NWs uniformly covered with high-density TiO₂ NRs that grew laterally out of the side surfaces. Inset is an SEM image of the Si NWs fabricated by deep RIE using nanosphere monolayer as a mask. (b) Cross-section of TiO₂ NRs-coated Si NW arrays, where the lengths of Si NWs were $\sim 15 \mu\text{m}$. (c,d) The middle and bottom portions of Si NWs showing dense and uniform coating of TiO₂ NRs along the entire NW length.

NRs could be found filling all these spaces. These TiO₂ NRs are $30 \pm 6 \text{ nm}$ in diameter and $243 \pm 31 \text{ nm}$ in length statistically. Figure 4b shows that the Si NWs were $\sim 25 \mu\text{m}$ in length, where the top portions (a few μm long) were bundled together. Below the bundles, Si NWs are evenly distributed providing a good template for conformal NRs growth. Higher-magnification SEM images acquired along the length direction of the Si NWs forest confirmed the dense and uniform coverage of these NRs. Figure 4c,d are two representative images indicating the density and dimensions of TiO₂ NRs were nearly identical at the middle and bottom regions. The NRs grew out laterally from the Si NWs and filled out the interspaces. Thus, considerably large surface area and high porosity were created by such a 3D architecture.

Undoped TiO₂ by vapor deposition usually appears *n*-type semiconductor due to intrinsic defects such as O vacancies and/or

Ti interstitials.^{34,35} When in contact with *n*-type Si, the band structure of TiO₂ will likely be reconfigured. The predicted equilibrium band alignment is schematically shown in Figure 5a. An electron accumulation region and a hole accumulation region are expected to appear on the TiO₂ and Si sides of the interface.^{20,28} Upon illumination, electron–hole pairs can be generated in both TiO₂ and Si. The TiO₂ NRs or polycrystalline films only absorb light below 420 nm (Supporting Information Figure S4). Thus, most visible light is still available for Si to absorb. Preferable band bending between TiO₂ and electrolyte directs photogenerated holes in TiO₂ toward the TiO₂/electrolyte interface that in turn oxidize OH[−] ions in solution into O₂. Meanwhile, photogenerated electrons in Si flow to the counter electrode for H₂O reduction. The charge accumulation regions at the TiO₂/Si interface attract photogenerated electrons from TiO₂ and holes from Si. Thus,

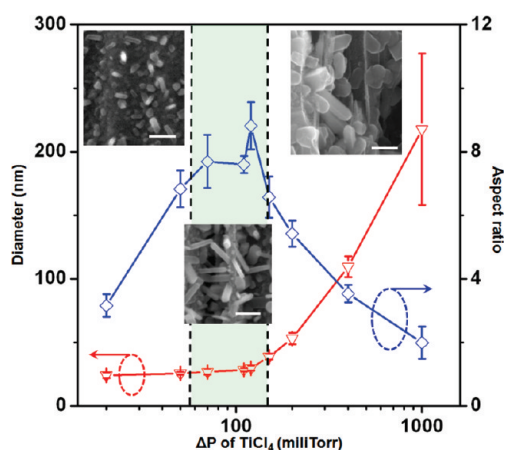


Figure 3. Plot of TiO₂ NR diameter and aspect ratio versus pressure fluctuation of TiCl₄ precursor. The light green zone between two dashed lines presents the optimal pressure change for growing TiO₂ NRs inside Si NW forests. Representative morphologies of TiO₂ nanocrystals grown with under-exposure, proper-exposure, and overexposure of TiCl₄ precursor are shown in the left, middle, and right insets, respectively.

quick recombination of these charge carriers at the interface completes the charge flow circuit. It is believed that n-TiO₂/n-Si band alignment is beneficial for electron–hole separation in TiO₂ and would contribute to the enhancement of photoanodic current.^{20,28} Furthermore, greatly increased surface area of NRs of TiO₂ should help to ensure efficient collection of photoenergy and boost the performance of PEC cells.

Prior to applying the TiO₂ NR-Si NW architecture to PEC system, an additional layer of anatase TiO₂ polycrystalline thin film was deposited by ALD (typically 250–400 cycles) to completely cover the Si surfaces and prevent the contact between Si and electrolyte. Furthermore, in order to provide for a comparison in performance, a reference sample was produced by coating an as-fabricated wet-etched Si NWs with a thin film of anatase TiO₂ via ALD. The deposition temperature was 300 °C and SEM observation showed that the polycrystalline film had grain sizes ranging from ~10 to 50 nm (see Supporting Information Figure S5).

PEC characterizations were performed in a 1 M KOH electrolyte using a typically three-electrode electrochemical cell configuration. The schematic setup is shown in Supporting Information Figure S6. TiO₂ NR-Si NW 3D architectures or TiO₂ film-Si NWs heterostructures (for comparison) were used as the working electrode; Pt wire served as the counter electrode; and a saturated calomel electrode (SCE) was used as the reference electrode. All three electrodes were immersed in a Teflon cell on which a quartz window was installed for light illumination. N₂ gas was purged through the cell during the measurement to instantaneously flush away O₂ from the working electrode and H₂ from the counter electrode. A light source with intensity of 100 mW/cm² was provided by a 500 W Hg (Xe) arc lamp (Oriel, 66142). A liquid water filter (Oriel, 6123NS) was applied to eliminate the IR light heating effect on electrolyte.

A typical plot of photocurrent density versus bias potential is shown in Figure 5b. It was taken from a 10 μm long dry-etched Si NW sample covered with TiO₂ NRs plus an additional 375-cycle TiO₂ overcoating. Interrupted illumination was applied to demonstrate the instant dark current and photocurrent density. The dark current density remained at a very low level (<10⁻² mA/cm²) under bias potentials between -1.2 and 0.5 V

(vs SCE) indicating the high quality of the crystal surfaces of TiO₂. From the plot, three regions can be clearly identified: a plateau of photocurrent density at bias potentials >-0.7 V (vs SCE) corresponding to the saturation of photogenerated holes; an inclining photocurrent density region at bias potentials ranging from -1.0 (the open circuit voltage, V_{OC}) to -0.7 V (vs SCE); and a zero photocurrent density region where the negative bias potential (<-1.0 V vs SCE) was close to that of the flat band potential. The *J*-*E* curve exhibited a fill factor of 0.54 and short circuit current density (*J*_{SC}) of 1.14 mA/cm², which demonstrated good charge transport properties and interfacial reaction chemistries of these 3D TiO₂ NR-Si NW anodes. All the photocurrent was contributed by the TiO₂ NRs due to their complete coverage on Si NWs, as shown by the incident photon to charge carrier efficiency (IPCE) curve, where the cutoff wavelength of IPCE was found well aligned with the TiO₂ absorption edge at ~420 nm (Supporting Information Figure S7).

To further demonstrate the merits of the 3D NW networks as PEC anodes, performance of three TiO₂-Si NW-based configurations were characterized and compared. They are wet-etched Si NWs with TiO₂ NRs, dry-etched Si NWs with TiO₂ NRs, and wet-etched Si NWs coated with a 375-cycle TiO₂ film. Both TiO₂ NR-Si NW samples were further overcoated with an additional 375-cycle TiO₂ film. All the Si NW templates were 10 μm long. Figure 5c shows the photocurrent density of these three samples as functions of the bias potential. The three plots followed the same trend and exhibited the same V_{OC}, while *J*_{SC} of these samples were dramatically different. The TiO₂ thin-film-coated Si NWs produced a *J*_{SC} of ~0.66 mA/cm², which is comparable to the value reported by others.²⁰ Both NRs-coated samples exhibited significantly higher *J*_{SC} owing to their larger surface areas. Because the density of wet-etched Si NWs was higher than that of dry-etched Si NWs, it yielded the highest *J*_{SC} (~1.43 mA/cm²), which was more than twice of what was produced by the thin-film-coated sample.

Photoelectrochemical efficiencies were also evaluated via the equation

$$\eta(\text{photo})\% = \left[j_p(E_{\text{rev}}^0 - |E_{\text{bias}} - E_{\text{aoc}}|) \frac{100}{I_0} \right]$$

where *j_p* is the photocurrent density, *E*_{rev}⁰ is the standard state-reversible potential (1.23 V for water-splitting reaction), *E*_{bias} is the bias potential at which *j_p* is measured, and *E*_{aoc} is the bias potential at open circuit (-1.0 V when SCE and 1 M KOH electrolyte are applied). The calculated efficiencies of the TiO₂ film-wet-etched-Si NW sample were plotted as a function of biasing potential (Supporting Information Figure S8), where the maximum efficiency (0.42%) was identified at ~-0.65 V of bias. Through this method, efficiencies of NRs-wet-etched-NWs and NRs-dry-etched-NWs were found to be 0.86 and 0.70%, respectively (Supporting Information Figure S8). Although the absolute values were not significantly high, they were already 105 and 67% higher than the core-shell NW configuration. This result suggests that the surface area of TiO₂ likely played a significant role in improving the photocatalyzed water splitting efficiency.

Dependence of photocurrent density on the length of Si NW backbones is shown in Figure 6a. Here, 1.5, 10, and 20 μm long Si NW-based 3D architectures were prepared followed by 375-cycle TiO₂ overcoating. Longer Si NW-based 3D structure provided higher photocurrent density. It should be noted that current

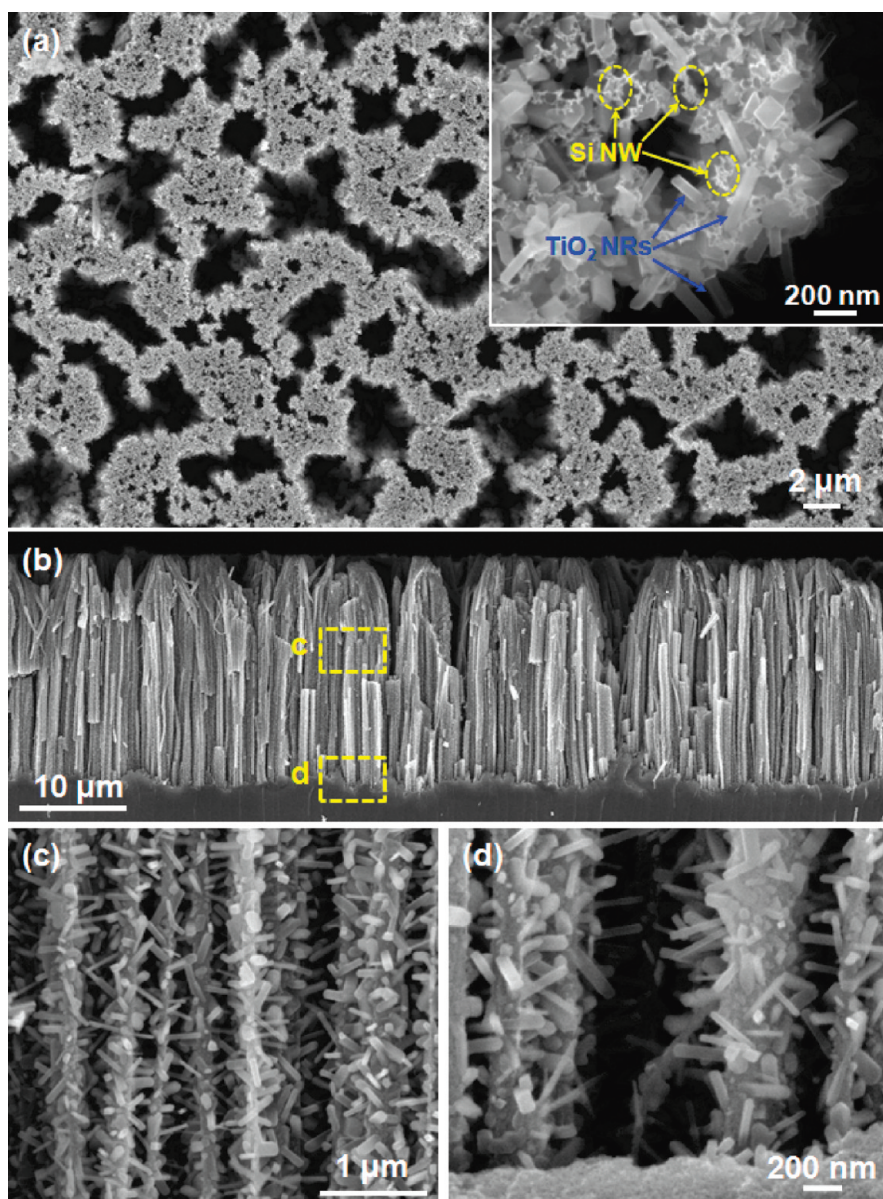


Figure 4. TiO₂ NRs grown on vertical Si NW arrays fabricated by wet etching. (a) Top view of Si NWs after TiO₂ NR growth. Bundling of NW tips was due to capillary attraction during wet etching. Inset is a higher-magnification SEM image showing TiO₂ NRs growing laterally around Si NWs. (b) Cross-section of vertical Si NW arrays covered with TiO₂ NRs. The Si NWs are $\sim 25 \mu\text{m}$ long and the top $\sim 5 \mu\text{m}$ region was bundled together. (c,d) The middle and bottom portions of Si NWs showing dense and uniform coverage of TiO₂ NRs along the entire NW length.

density per unit length of 10 and 20 μm Si NWs was lower than that of the 1.5 μm sample, although the size and density distribution of the TiO₂ NRs was nearly identical. This nonlinear increase of photocurrent is possibly related to the difficulty of removing O₂ from deep inside the 3D NW forest. Efficiency calculations showed that the 20 μm sample had a three times higher efficiency than the 1.5 μm one suggesting the performance enhancement resulted from an increase of surface area (Table 1).

TiO₂ overcoating was a necessary treatment in order to isolate Si from the electrolyte and achieve a stable PEC anode. However, one should caution that the overcoating thickness might also alter PEC performance. To demonstrate the overcoating influence, 250 and 375 ALD cycles of overcoating were applied to TiO₂ NRs-covered wet-etched Si NW arrays with two different lengths (10 and 20 μm). Figure 6b illustrates the corresponding

$J-E$ curves of these four different samples. The sample conditions, J_{SC} , and efficiencies (derived from Supporting Information Figure S8) are also summarized in Table 1. It was found that the sample with the 250-cycle overcoating produced higher photocurrent than the ones with a 375-cycle of overcoating. The highest efficiency (2.1%) was identified from the 20 μm sample with the 250-cycle overcoating. This is a competitive value as compared to other TiO₂-based PEC anodes.^{4,10,14,20,22,23,25,26,28,29,36,37}

In order to provide a visual interpretation for these performance changes, the morphology of the overcoatings was investigated by SEM. As shown in Figure 6c,d, diameters of the TiO₂ NRs were nearly unaffected after overcoating. However, the observable lengths of the NRs were clearly shortened when the overcoating cycles increased from 250 to 375 (Figure 6c, d). This observation suggests that the 300 °C TiO₂ ALD did not provide a

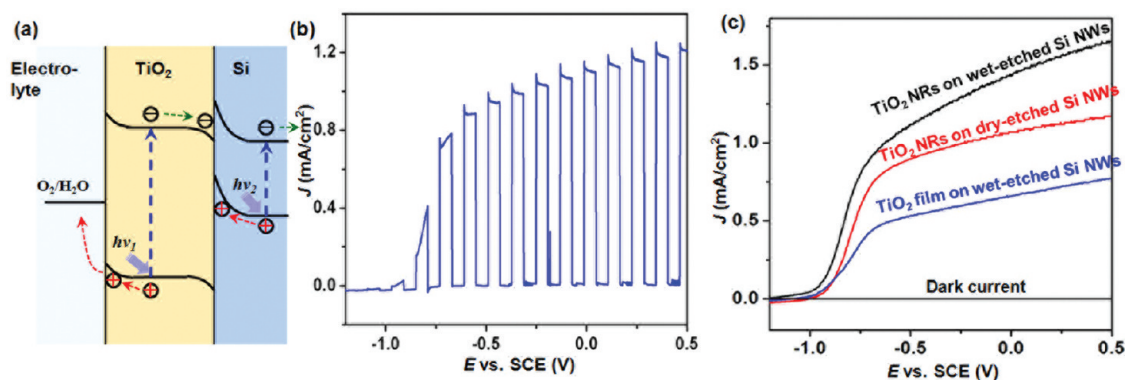


Figure 5. PEC performance of TiO₂ NR-Si NW heterostructures. (a) Schematic band diagram of an n-TiO₂/n-Si heterojunction and corresponding charge transfer when applied as a PEC anode. (b) J - E curve of TiO₂ NR on 10 μm dry-etched Si NW under interrupted illumination. (c) J - E curves and dark currents of different TiO₂-Si NW configurations showing enhanced PEC performance by introducing high-density TiO₂ NR branches.

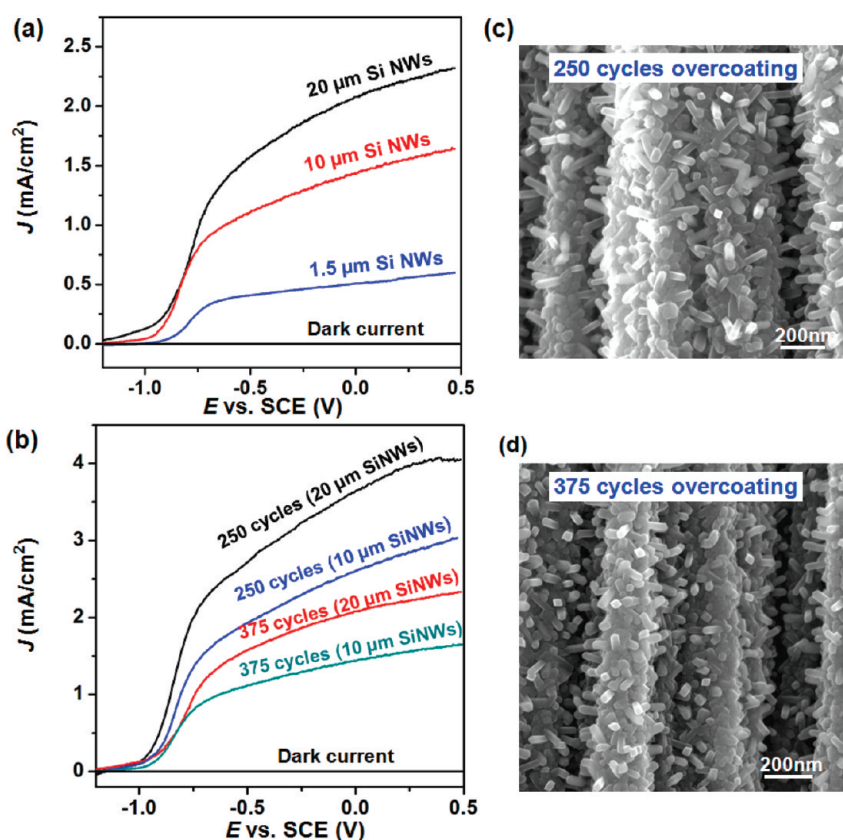


Figure 6. PEC performance analysis of 3D TiO₂ NR-Si NW architectures. (a) Si NW length-dependent photocurrent densities and dark currents, where TiO₂ NRs from these three samples were grown under the same condition exhibiting the same size and density distribution, and all samples were overcoated by additional 375 cycles of TiO₂ ALD at 300 °C. (b) J - E curves and dark currents of TiO₂ NR-Si NW PEC anodes with different lengths and overcoating cycles. (c,d) SEM images of TiO₂ NR-Si NW structures after 250 and 375 cycles ALD overcoating, respectively. More overcoating cycles buried more TiO₂ NRs in the TiO₂ film.

conformal coating over all surfaces but rather a deposition around the roots of TiO₂ NRs and on the exposed surfaces of Si NWs. Therefore, the direct consequence of increasing overcoating cycles was to “bury” more NRs in the TiO₂ film and decrease the overall surface area of TiO₂ crystals. Another possible reason for changes in performance with respect to overcoatings could be the shrinkage of porosity of the 3D structure. Thick coatings around the NWs significantly reduce the open space in the NW-NR 3D structure.

This would likely hinder the release of O₂ and impede the PEC reactions of OH⁻ oxidation.

In conclusion, we have developed a high-density 3D hierarchical NW architecture for efficient PEC electrodes. The TiO₂ NRs-Si NWs network structure offers large surface areas, good charge transport properties, and large porosities. A 2.1% photoelectrochemical efficiency was obtained from such a 3D NW architecture, which is three times higher than that of TiO₂ film-Si

Table 1. Summary of Photocurrent Density and Photoelectrochemical Efficiency of TiO₂–Si Heterostructures

type of Si NWs	length (μm)	TiO ₂ NRs	overcoating cycles	J_{sc} (mA/cm ²)	η (%)
wet-etched	20	yes	250	3.64	2.10
wet-etched	10	yes	250	2.62	1.47
wet-etched	20	yes	375	2.08	1.20
wet-etched	10	yes	375	1.43	0.86
dry-etched	10	yes	375	1.07	0.70
wet-etched	1.5	yes	375	0.51	0.32
wet-etched	10	no	375	0.66	0.42

NWs core–shell structure. This comparison suggests that the 3D NW architecture is likely superior to straight NW arrays for PEC electrode design. The efficiency could be further improved by optimizing the number of overcoating cycles and the length/density of NW backbones. We are also aware that although the heterojunction between n-TiO₂ and n-Si is favorable for electron–hole separation, this configuration requires the absorption of an additional photon to complete one redox reaction, as evidenced by the $\sim 50\%$ IPCE near the absorption edge (Supporting Information Figure S7). This could be an ultimate limit for improvement with respect to efficiencies. This limitation might be solved by selecting metallic 1D backbones to replace Si NWs and is not in conflict with the merits of the 3D NW architectures we have demonstrated in this paper. This technique opens a new avenue toward high-performance electrodes using high-density 3D NW networks and could show substantial impacts on PEC and photovoltaic devices design and improvement.

■ ASSOCIATED CONTENT

S Supporting Information. Additional information of detailed experimental procedures and measurement setups and figures of crystal structural analysis, wet-etched Si NWs and TiO₂ film coating, IPCE, and photoelectrochemical efficiency profiles. This material is available free of charge via the Internet at <http://pubs.acs.org>.

■ AUTHOR INFORMATION

Corresponding Author

*E-mail: xudong@engr.wisc.edu.

■ ACKNOWLEDGMENT

We thank National Science Foundation under Grant CMMI-0926245 and UW-Madison graduate school.

■ REFERENCES

- (1) Fujishima, A.; Honda, K. *Nature* **1972**, *238*, 37–38.
- (2) Gratzel, M. *Nature* **2001**, *414*, 338–344.
- (3) Bak, T.; Nowotny, J.; Rekas, M.; Sorrell, C. C. *Int. J. Hydrogen Energy* **2002**, *27*, 991–1022.
- (4) Chen, X. B.; Shen, S. H.; Guo, L. J.; Mao, S. S. *Chem. Rev.* **2010**, *110*, 6503–6570.
- (5) Currao, A. *Chimia* **2007**, *61*, 815–819.
- (6) Maeda, K.; Domen, K. *J. Phys. Chem. Lett.* **2010**, *1*, 2655–2661.
- (7) Su, J. Z.; Feng, X. J.; Sloppy, J. D.; Guo, L. J.; Grimes, C. A. *Nano Lett.* **2011**, *11*, 203–208.

- (8) Walter, M. G.; Warren, E. L.; McKone, J. R.; Boettcher, S. W.; Mi, Q. X.; Santori, E. A.; Lewis, N. S. *Chem. Rev.* **2010**, *110*, 6446–6473.
- (9) Kohl, P. A.; Frank, S. N.; Bard, A. J. *J. Electrochem. Soc.* **1977**, *124*, 225–229.
- (10) Morisaki, H.; Watanabe, T.; Iwase, M.; Yazawa, K. *Appl. Phys. Lett.* **1976**, *29*, 338–340.
- (11) Nakato, Y.; Yano, H.; Nishiura, S.; Ueda, T.; Tsubomura, H. *J. Electroanal. Chem.* **1987**, *228*, 97–108.
- (12) Nozik, A. J. *Appl. Phys. Lett.* **1977**, *30*, 567–569.
- (13) Peng, K. Q.; Wang, X.; Wu, X. L.; Lee, S. T. *Nano Lett.* **2009**, *9*, 3704–3709.
- (14) Shankar, K.; Basham, J. I.; Allam, N. K.; Varghese, O. K.; Mor, G. K.; Feng, X. J.; Paulose, M.; Seabold, J. A.; Choi, K. S.; Grimes, C. A. *J. Phys. Chem. C* **2009**, *113*, 6327–6359.
- (15) Wagner, S.; Shay, J. L. *Appl. Phys. Lett.* **1977**, *31*, 446–447.
- (16) Chen, X. B.; Liu, L.; Yu, P. Y.; Mao, S. S. *Science* **2011**, *331*, 746–750.
- (17) Boettcher, S. W.; Spurgeon, J. M.; Putnam, M. C.; Warren, E. L.; Turner-Evans, D. B.; Kelzenberg, M. D.; Maiolo, J. R.; Atwater, H. A.; Lewis, N. S. *Science* **2010**, *327*, 185–187.
- (18) Boettcher, S. W.; Warren, E. L.; Putnam, M. C.; Santori, E. A.; Turner-Evans, D. B.; Kelzenberg, M. D.; Walter, M. G.; McKone, J. R.; Brunschwig, B. S.; Atwater, H. A.; Lewis, N. S. *J. Am. Chem. Soc.* **2011**, *133*, 1216–1219.
- (19) Hanna, M. C.; Nozik, A. J. *J. Appl. Phys.* **2006**, *100*, 074510(1)–074510(8).
- (20) Hwang, Y. J.; Boukai, A.; Yang, P. D. *Nano Lett.* **2009**, *9*, 410–415.
- (21) Kelzenberg, M. D.; Boettcher, S. W.; Petykiewicz, J. A.; Turner-Evans, D. B.; Putnam, M. C.; Warren, E. L.; Spurgeon, J. M.; Briggs, R. M.; Lewis, N. S.; Atwater, H. A. *Nat. Mater.* **2010**, *9*, 368–368.
- (22) Kim, J. H.; Yun, T. K.; Bae, J. Y.; Ahn, K. S. *Jpn. J. Appl. Phys.* **2009**, *48*, 120204(1)–120204(3).
- (23) Park, J. H.; Kim, S.; Bard, A. J. *Nano Lett.* **2006**, *6*, 24–28.
- (24) Yin, W. J.; Tang, H. W.; Wei, S. H.; Al-Jassim, M. M.; Turner, J.; Yan, Y. F. *Phys. Rev. B* **2010**, *82*, 045106(1)–045106(6).
- (25) Sakthivel, S.; Janczarek, M.; Kisch, H. *J. Phys. Chem. B* **2004**, *108*, 19384–19387.
- (26) Sene, J. J.; Zeltner, W. A.; Anderson, M. A. *J. Phys. Chem. B* **2003**, *107*, 1597–1603.
- (27) Shen, X. J.; Sun, B. Q.; Yan, F.; Zhao, J.; Zhang, F. T.; Wang, S. D.; Zhu, X. L.; Lee, S. *ACS Nano* **2010**, *4*, 5869–5876.
- (28) Takabayashi, S.; Nakamura, R.; Nakato, Y. *J. Photochem. Photobiol., A* **2004**, *166*, 107–113.
- (29) Mahajan, V. K.; Misra, M.; Raja, K. S.; Mohapatra, S. K. *J. Phys. D: Appl. Phys.* **2008**, *41*, 125307(1)–125307(9).
- (30) Shi, J.; Sun, C. L.; Starr, M. B.; Wang, X. D. *Nano Lett.* **2011**, *11*, 624–631.
- (31) Shi, J.; Wang, X. D. *Cryst. Growth Des.* **2011**, *11*, 949–954.
- (32) Garnett, E.; Yang, P. D. *Nano Lett.* **2010**, *10*, 1082–1087.
- (33) Jeong, S.; Hu, L. B.; Lee, H. R.; Garnett, E.; Choi, J. W.; Cui, Y. *Nano Lett.* **2010**, *10*, 2989–2994.
- (34) Carp, O.; Huisman, C. L.; Reller, A. *Prog. Solid State Chem.* **2004**, *32*, 33–177.
- (35) Diebold, U. *Surf. Sci. Rep.* **2003**, *48*, 53–229.
- (36) Sakata, T.; Kawai, T.; Hashimoto, K. *Chem. Phys. Lett.* **1982**, *88*, 50–54.
- (37) Wang, X. W.; Liu, G.; Wang, L. Z.; Pan, J. A.; Lu, G. Q.; Cheng, H. M. *J. Mater. Chem.* **2011**, *21*, 869–873.